An Ultra-Low-Loss Waveguide Based on BIC Used for an On-Chip Integrated Optical Gyroscope

Zhenkun Yuan [1,2], Jian Chen [2], Dingbo Chen [2], Shuolong Zhu [1], Junbo Yang [2,*] and Zhenrong Zhang [1,*]

1   Guangxi Key Laboratory of Multimedia Communications and Network Technology, School of Computer, Electronics and Information, Guangxi University, Nanning 530004, China
2   College of Sciences, National University of Defense Technology, Changsha 410073, China
*   Correspondence: yangjunbo@nudt.edu.cn (J.Y.); zzr76@gxu.edu.cn (Z.Z.)

Abstract: The development of integrated optical technology and the continuous emergence of various low-loss optical waveguide materials have promoted the development of low-cost, size, weight, and power optical gyroscopes. However, the losses in conventional optical waveguide materials are much greater than those in optical fibers, and different waveguide materials often require completely different etching processes, resulting in severely limited gyroscope performance, which is not conducive to the monolithic integration of gyroscope systems. In this paper, an ultra-low-loss Archimedean spiral waveguide structure is designed for an on-chip integrated optical gyroscope by using the high Q value and low-loss optical characteristics of the bound state in the continuum (BIC). The structure does not require the etching of high-refractive-index optical functional materials, avoiding the etching problem that has been difficult to solve for a long time. In addition, the optical properties of the BIC straight and the BIC bent waveguide are simulated using the finite element method (FEM) to find the waveguide structural parameters corresponding to the BIC mode, which is used to design the integrated sensing coil and analyze the gyroscope performance. The simulation results show that the gyroscope's sensitivity can reach $0.6699°/s$. This research is the first time a BIC optical waveguide has been used for an integrated optical gyroscope, providing a novel idea for the monolithic integration of optical gyroscopes.

Keywords: optical waveguide; ultra-low-loss; integrated optical gyroscope; bound state in the continuum; finite element method; integrated sensing coil

1. Introduction

Optical gyroscopes based on the Sagnac effect are widely used in inertial navigation, weaponry, space vehicles, marine exploration, automotive navigation, robot control, and other industrial applications due to their high accuracy, lack of moving parts, high stability, long service life, and high resistance to electromagnetic interference [1,2]. Ring laser gyroscopes (RLGs) and fiber optic gyroscopes (FOGs) dominate the optical gyroscope market. Although both of these optical gyroscopes offer high levels of accuracy, their large size, high cost, and high power consumption limit their use in integrated devices for a wide range of portable applications [3–5]. With the increasing demands for inertial sensing systems in the future market, on-chip integrated optical gyroscopes with low cost, size, weight, and power will become the research focus of the next generation of optical gyroscopes [6].

The sensitive component of an integrated optical gyroscope is sensitive to the Sagnac effect by using an optical waveguide spiral coil instead of a fiber coil. At the same time, other optoelectronic devices are integrated on a chip using a monolithic or optoelectronic hybrid integration process, which significantly reduces the system's size, weight, and cost. It is the further miniaturization of a laser gyroscope and a fiber optic gyroscope, so it is also called a "gyroscope on-chip" [7]. However, due to the small space size and the loss of

the planar optical waveguide being much larger than that of the optical fiber, the optical waveguide coil is difficult to design to be very long, which leads to a severe limitation of gyroscope performance. How to extend the optical path and reduce the waveguide loss in the limited space to enhance the Sagnac effect is particularly important. The interferometric integrated optical gyroscope realizes the determination of the rotational angular velocity by measuring the phase difference formed by the interference of two back-propagation beams in the sensing loop caused by the Sagnac effect. As the core sensitive component of the integrated optical gyroscope, the passive sensitive loop's performance directly affects the gyroscope system's overall performance. The design and fabrication of a low-loss sensitive loop is the main research content to improve the performance of an integrated optical gyroscope [8,9].

In order to reduce losses of optical waveguide materials and improve their integration, the integration platforms of passive sensitive loops for integrated optical gyroscopes have been extensively investigated in recent years. The research results of using indium phosphorus (InP) [10–12], silicon on insulator (SOI) [13–15], silicon nitride (Si_3N_4) [16–20], silicon dioxide (SiO_2) [21–24], polymers [25,26], lithium niobate ($LiNbO_3$) [27,28], and calcium fluoride (GaF_2) [29,30] for the fabrication of optical waveguide structures have been reported. In addition, Brunetti et al. designed an ultra-high Q-factor 1D-PhC ring resonant cavity based on Si_3N_4 material, achieving an ultra-high Q-factor ($>10^9$) with a footprint of 16 mm^2. This performance makes the 1D-PhCRR applicable to integrated optical gyroscopes [31]. Liu et al. achieved ultra-low-loss waveguides based on silicon nitride (Si_3N_4) waveguide materials on a CMOS integrable 200 mm wafer platform with a loss of 0.034 dB/m, accelerating the development of high-performance photonic integration [32]. Although the losses of these traditional integrated optical waveguide platforms are much lower than before, the performances of these platforms for designing integrated optical gyroscopes are not ideal, so further loss reduction is needed. Moreover, these traditional optical waveguide structures usually require complex etching processes, which are not conducive to the large-scale production of gyroscopes.

The proposed bound states in the continuum (BICs) provide a viable solution to the above problem. BICs have recently been studied and widely used in nanophotonics. They refer to the intermittent existence of some frequencies in the continuous spectrum of free radiation that can be bound near the waveguide without propagating freely into the distance. Some optical modes in BICs can coexist with modes of optical radiation in free space, specific momentum, and frequency. Although their frequencies are in the radiation continuum domain, they are not coupled to the radiation wave and are strictly bound within the waveguide like guided wave modes. The bound state in the continuum (BIC) is considered to be a physical phenomenon that differs from the traditional view of fluctuation theory, i.e., a singular phenomenon that does not obey the premise of total internal reflection without radiation [33]. By designing specific waveguide structures, it is theoretically possible to achieve optical standing waves and zero-loss transmission. The optical gyroscopes designed using BIC waveguides have higher stability and precision compared to traditional optical gyroscopes. This is because BIC waveguides have the characteristics of zero-loss transmission and ultra-high quality factors, which can reduce optical loss and noise, improving measurement sensitivity and stability. Additionally, the compact structure and high integration of BIC waveguides can also achieve smaller volumes and higher integration, thereby improving device reliability and application range.

In this paper, an ultra-low-loss spiral waveguide structure is designed and applied to an interferometric integrated optical gyroscope system based on the optical BIC's unique mechanism and principle. The structure uses an easily processed low-refractive-index polymer material as the optical waveguide. By theoretically designing the geometry structure of the low-refractive-index optical waveguide, a continuous bound state is obtained so that the photon is effectively bound to the high-refractive-index functional material directly below the low-refractive-index waveguide, resulting in ultra-low-loss transmission. Compared with the waveguide structure of traditional materials, the propagation loss of

the BIC waveguide structure is significantly reduced, and the Q value of the waveguide is improved. Since this optical waveguide structure eliminates the need for the etching of optical modules with high refractive indices and avoids the long-standing problem of etching, it is possible to develop integrated optical chips based on arbitrary optical functional materials using this optical waveguide structure. Thereinto, the relatively small winding length of the low-loss Archimedean spiral coil creates a large effective area, making it possible for the miniature sensor to measure low rotational speeds and ensuring that the optical gyroscope has high sensitivity while maintaining miniaturization. This research is the first time a BIC optical waveguide has been used for an integrated optical gyroscope, providing a novel idea for the monolithic integration of optical gyroscopes. The work is conducive to promoting the application of BIC in gyroscopes and further promoting the development of gyroscopes in related fields.

2. Model and Theory

A three-dimensional schematic of the Archimedean spiral waveguide structure we have designed is shown in Figure 1a, which is connected by some straight and bent waveguides that support the BIC mode and act as an integrated sensing coil for the gyroscope. Figure 1b shows the cross section of the spiral waveguide structure. In Figure 1b, the heights of the low-refractive-index polymer waveguide, high-refractive-index thin-film silicon (Si) layer, and silicon dioxide (SiO_2) substrate are fixed as constant t = 500 nm, h = 400 nm, and H = 2.0 μm, respectively, where w is the width of the polymer waveguide. and its value is determined by subsequent simulations to be 1.336 μm. The refractive indices of the above three materials are 1.54, 3.48, and 1.44, respectively. Figure 1c describes the basic principle diagram of the interferometric integrated optical gyroscope based on the BIC structure, which includes the front end of the gyroscope and the integrated sensitive coil. The light emitted by the light source is equally divided into two beams by the 3 dB coupler after passing through the circulator, forming clockwise (CW) and counterclockwise (CCW) beams in the integrated sensitive coil and propagating in opposite directions. As the gyroscope rotates perpendicular to the plane, the two counter-propagating beams pass through different phase shifts, which are proportional to the angular velocity of the rotation. Finally, they interfere at the 3 dB coupler, where the phase shift is converted into intensity information, and the two photodetectors detect the output with the assistance of a circulator.

The phase modulator is an essential component of the interferometric gyroscope as it regulates the optimally sensitive operating bias of the gyroscope. In designing and manufacturing optical gyroscopes, it is critical to ensure that no cross-coupling occurs between the CW and CCW modes. By modulating the phase of the input light using a phase modulator, a specific phase difference exists between the CW and CCW directions during propagation. As these signals originate from the phase modulator, their phase difference can be precisely controlled. By keeping the phase difference between the two counterpropagating modes constant, interference between them can be avoided, given that their interference patterns differ when the phase difference between the CW and CCW directions varies. Therefore, the phase difference between the CW and CCW modes along the same loop remains unchanged, effectively preventing cross-coupling and improving the accuracy and sensitivity of the optical gyroscope.

The principle of BIC can be explained by the bound-state model of quantum mechanics. In quantum mechanics, a bound state is a state whose energy is lower than that of a continuum state, where an electron is bound around the nucleus. The energy of the BIC mode is also lower than that of the continuum state, but the photon in this state is not bound in the medium. Rather, it is restricted near the surface of the medium. This restriction is achieved through interference, which causes the scattering waves on the boundary to interfere with the waves inside the medium, forming a state near the surface of the medium with lower energy than the continuum state, that is, BIC. The difference between the BIC mode and the conventional localized mode is that the frequency of the BIC mode is in the

continuous spectrum, not the discrete mode, so its energy does not dissipate or propagate outside the medium.
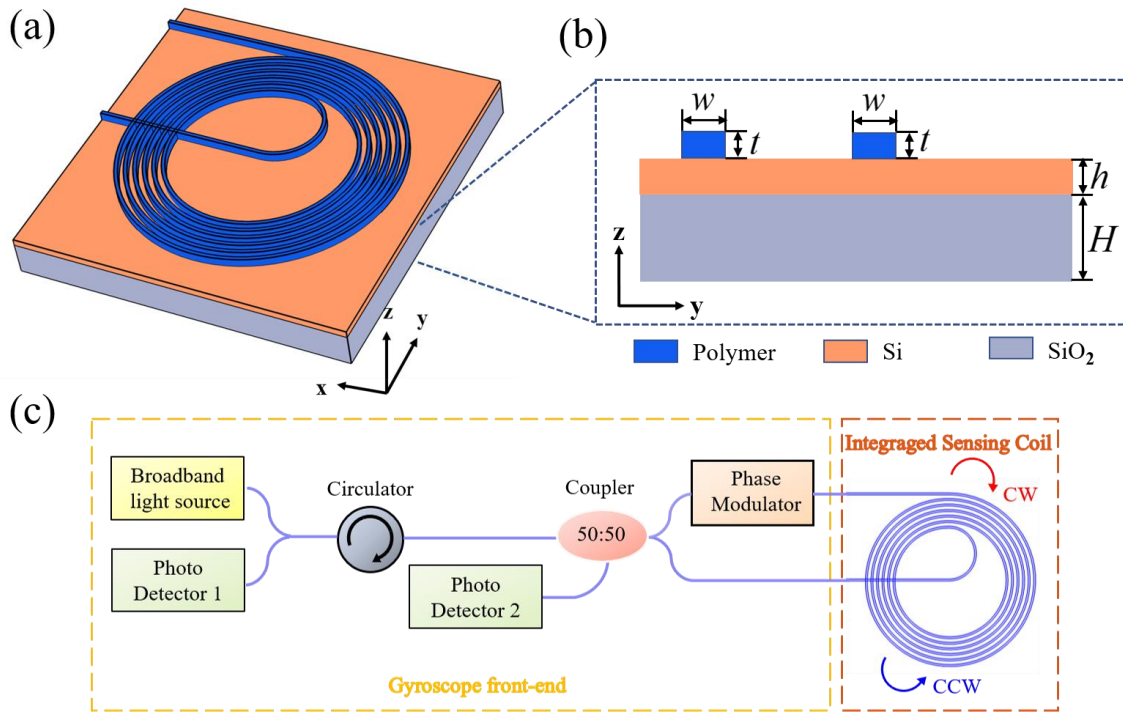
Figure 1. (**a**) Three-dimensional schematic of the Archimedean spiral waveguide structure supporting the BIC mode; (**b**) the cross-section diagram of the designed spiral waveguide structure; (**c**) the schematic diagram of the interferometric integrated optical gyroscope based on the BIC structure.

By solving the Schrödinger equation of a quantum system with a finite potential well, the eigenstates of the energy eigenvalues in the potential well can be obtained. These square integrable eigenstates are called bound states of quantum systems. Other states with eigenpotential energy above the potential well and wave function expanding to infinity are called continuous states, and the eigenvalues of their eigenstates are not square integrable [34–36]. In this paper, we use the BIC mechanism to avoid the photons in a TM bound mode being dissipated into the TE continuum through destructive interference between different coupling channels. Unlike traditional optical waveguide structures, the ideal BIC waveguide has zero propagation loss for certain geometric parameters. This physical phenomenon can be explained intuitively by the model shown in Figure 2.
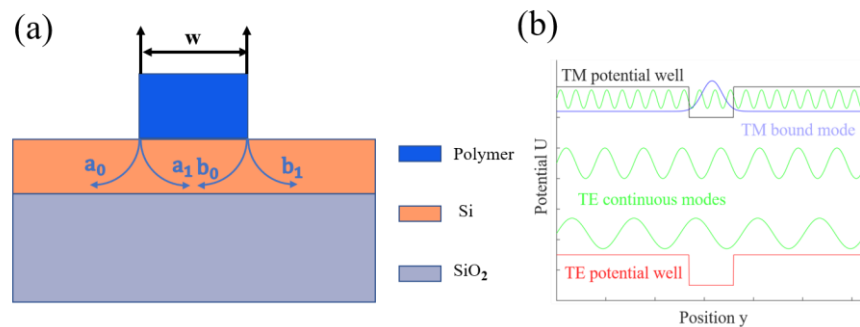
Figure 2. Theoretical analysis of the BIC hybrid waveguide structure. (**a**) The cross-section of the hybrid waveguide structure can support the BIC mode, which contains the radiation channels of the TM bound mode to the TE continuum; (**b**) photonic potential distribution of the hybrid waveguide structures.

In the hybrid waveguide structure shown in Figure 2a, the radiation loss of the TM bound mode to the TE continuum is formed at two edges of the waveguide. Each edge loss is caused by the coupling of the TM bound mode with the leftward (a_0 and b_0) and rightward (a_1 and b_1) TE continuous modes. When the losses in leftward (a_0 and b_0) and rightward (a_1 and b_1) interfere destructively and mutually cancel, then the total loss in the TM bound mode to the TE continuum can be reduced to zero, obtaining a lossless TM bound mode, which is the desired ideal BIC. The magnitude of the loss through leftward (a_0 and b_0) and rightward (a_1 and b_1) hinge on the phase difference caused by the waveguide width. Therefore, we can optimize the waveguide width to obtain the BIC structure we need. Figure 2b illustrates the potential photonic distribution of the waveguide structure shown in Figure 2a. The low-refractive-index polymer waveguide structure induces a potential well, resulting in a bound mode. The black and red lines indicate the potential wells of TM and TE polarized photons, respectively. There are many modes above the TE potential well where the green lines indicate some different TE continuous modes, and the blue line indicates a TM bound mode. The TM potential well can support a TM bound mode, and since the TM potential well lies above the TE potential well, the TM bound mode in the TM potential well lies in the continuous spectrum of the TE polarization.

The basic principle of optical gyroscopes is based on the Sagnac effect [36], i.e., when two light waves in a closed optical loop of arbitrary geometry, starting from any point and propagating in opposite directions, return to that point after one week of travel, the two light waves will produce a phase difference proportional to the angular velocity of rotation if the closed optical path rotates in a certain direction relative to the inertial space [37]. When the closed optical loop is stationary (Figure 3a), the optical paths of the CW and CCW beams transmitted for one week on the closed optical loop back to the origin S are the same. When the closed optical loop rotates along CW with angular velocity Ω (Figure 3b), the origin S becomes S', the optical paths passed in one week of CW transmission will be greater than those of the CCW beams, and the difference in optical paths between the two beams can be written as:
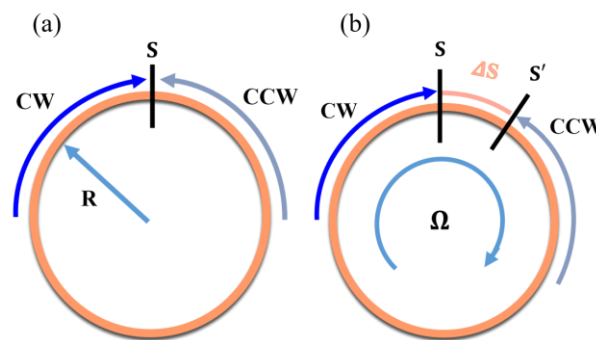
$$\Delta L = \frac{4A}{c} = 2\Delta S \tag{1}$$

Figure 3. Schematic diagram of the Sagnac effect in a circular light path: (**a**) the circular optical path is stationary; (**b**) the optical path rotates along clockwise with angular velocity Ω.

From the optical paths difference, we can derive the Saganc phase difference:

$$\Delta\phi = k \cdot \Delta L = \frac{2\pi}{\lambda} \cdot \frac{4A}{c}\Omega = \frac{8\pi A}{\lambda c}\Omega = \frac{4\pi RL}{\lambda c}\Omega \tag{2}$$

where A and L denote the effective area and length enclosed by the closed optical loop, respectively, c is the speed of light in vacuum, Ω is the rotational angular velocity, k is the wave vector, λ is the operating wavelength, R is radius of the closed loop, and ΔS represents the optical path change caused by rotation.

The optical signal detected by the photodetector is the result of interference between two beams of light propagating in opposite directions [38]. The optical power of the light

emitted from the source after passing through the spiral waveguide and reaching the two photodetectors can be expressed by the following expression:

$$P_{D1}(\varphi) = \frac{1}{2}P_0 10^{(-\gamma_{wg})/10}[1 + \cos(\varphi)] \tag{3}$$

$$P_{D2}(\varphi) = \frac{1}{2}P_0 10^{(-\gamma_{wg})/10}[1 - \cos(\varphi)] \tag{4}$$

where $\varphi = \Delta\phi + \varphi_0$, $\Delta\phi$ is the Sagnac phase difference, and φ_0 is the bias phase. In order to maximize the response of the gyroscope output to the rotation signal, the phase is biased to the maximum slope of the interferogram, i.e., set the phase bias $\varphi_0 = \pi/2$. The gyroscope can be kept working at the most sensitive point for the angular velocity by using phase modulation of the CW and CCW signals. When the gyroscope rotates ($\Delta\phi \neq 0$), the output power will change with the angular velocity Ω. When the gyroscope is stationary ($\Delta\phi = 0$), the optical power reaching the detector is a constant value. Substituting $\varphi_0 = \pi/2$ into Equations (3) and (4), then we can reach:

$$P_{Di} = \frac{1}{2}P_0 10^{(-\gamma_{wg})/10} = P_{D1} = P_{D2} \tag{5}$$

Among them, P_0 is the input optical power, $\gamma_{wg} = \alpha + 2N\gamma_x$ is the total loss of the spiral waveguide, L_n is the total length enclosed by the spiral waveguide, and N indicates the number of turns in the spiral waveguide. The multiplier in front of N indicates that the light passes through each crossroads twice, and α and γ_x denote the propagation loss and crossing loss of the spiral waveguide, respectively. According to the method described in Ref. [39], we simulated the transmission of a single waveguide crossing and obtained a loss of 0.04 dB for a single waveguide crossing point. The waveguide crossing loss γ_x is set to 0.04 dB/crossing in the later discussion.

In this paper, the mode analysis in COMSOL software is used to simulate the waveguide cross section. After setting the boundary conditions and meshing reasonably, the effective refractive index obtained from the mode analysis is a complex number whose imaginary part is usually used to characterize the transmission loss of the waveguide. The equation is given by [40]:

$$\alpha = -\frac{20}{\ln 10}\frac{2\pi}{\lambda}\gamma \approx -8.686\frac{2\pi}{\lambda}\gamma \text{ (dB/m)} \tag{6}$$

where λ is the operating wavelength, γ represents the effective refractive index imaginary part of the mode. Therefore, it is only necessary to calculate the imaginary part of the effective refractive index through simulation and bring it into the formula to obtain the waveguide loss.

The calculation of quality factor in BIC waveguide structure is also related to the effective refractive index of the mode. The complex form of the effective refractive index can be expressed as $n_{eff} = \omega_0 - i\gamma$, where the real part ω_0 represents the resonant frequency, and the imaginary part γ is the leakage rate. BIC is considered to be a special resonance with zero leakage and zero linewidth ($\gamma = 0$). The quality factor (Q) can be defined as [41]:

$$Q = \frac{\omega_0}{2\gamma} \tag{7}$$

3. Simulations and Analysis

In order to design the Archimedean spiral waveguide structure supporting the BIC mode, the corresponding waveguide structure parameters in the BIC mode are found to determine the necessary parameters for the abovementioned integrated sensing coil design. We use COMSOL software based on finite element analysis to simulate the optical properties of the hybrid waveguide structure we have designed. Figure 4a,b show the

electric field $|E|$ distribution of the TM bound mode and a TE continuous mode supported by the hybrid waveguide structure in Figure 2a. The electric field energy of the TM bound mode is only confined to the high-refractive-index substrate under the low-refractive-index waveguide. However, for a TE continuous mode, the electric field expands in the high-refractive-index substrate, resulting in the dissipation of the propagating photons. To study the ultra-low-loss characteristics of hybrid waveguide structures, we chose TM bound modes as the main research mode for our study in this paper.
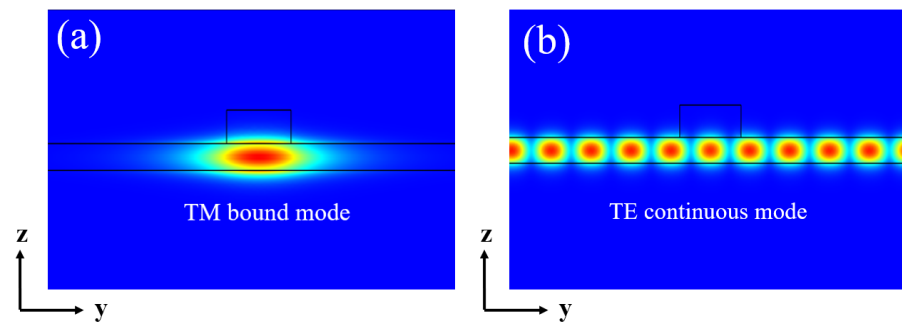

Figure 4. The electric field $|E|$ distribution of (**a**) the TM bound mode and (**b**) a TE continuous mode.

The vertical $|E_z|$ and horizontal $|E_y|$ electric field distributions in the TM bound mode are depicted in Figure 5a,b, respectively. The existence of the horizontal electric field component indicates a small part of the TE polarization component in the TM bound mode, which will be coupled with TE continuous modes in the high-refractive-index substrate to form a leakage-bound state. In a perfect TM bound mode, no coupling occurs between the purely electric field $|E_z|$ component and the purely electric field $|E_y|$ component since their modal overlap integral is zero. However, the waveguide structure we designed cannot transmit a perfect TM bound mode; therefore, this paper focuses on the optical properties of the waveguide structure supporting a quasi-TM bound mode. Our designed BIC waveguide structure typically has a high quality factor and ultra-low loss. Due to its unique optical properties, only one bound mode can be transmitted in the waveguide, which is the mono-modality. Therefore, we can ensure that the optical signal is transmitted only in a single mode, avoiding cross interference between different modes and improving the measurement accuracy and resolution of the gyroscope.
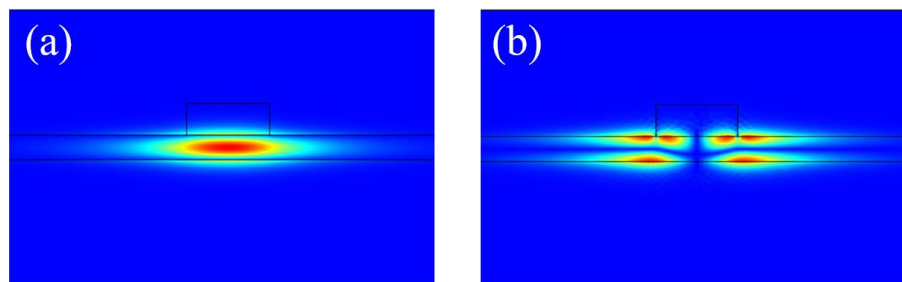

Figure 5. The electric field distribution of TM bound mode: (**a**) vertical component $|E_z|$; (**b**) horizontal component $|E_y|$.

3.1. BIC in a Straight Waveguide

In this paper, we first simulate and analyze the optical properties of the BIC under a straight waveguide structure. The simulation results in this paper are all based on a three-layer structure of the polymer, silicon (Si) layer, and silicon dioxide (SiO$_2$) substrate, as shown in Figure 6a, where the corresponding heights of the materials are 500 nm, 400 nm, and 2 μm, respectively. The refractive indices of the above three materials are 1.54, 3.48, and 1.44, respectively. Figure 6 shows the numerical simulation results of BIC in a straight waveguide.
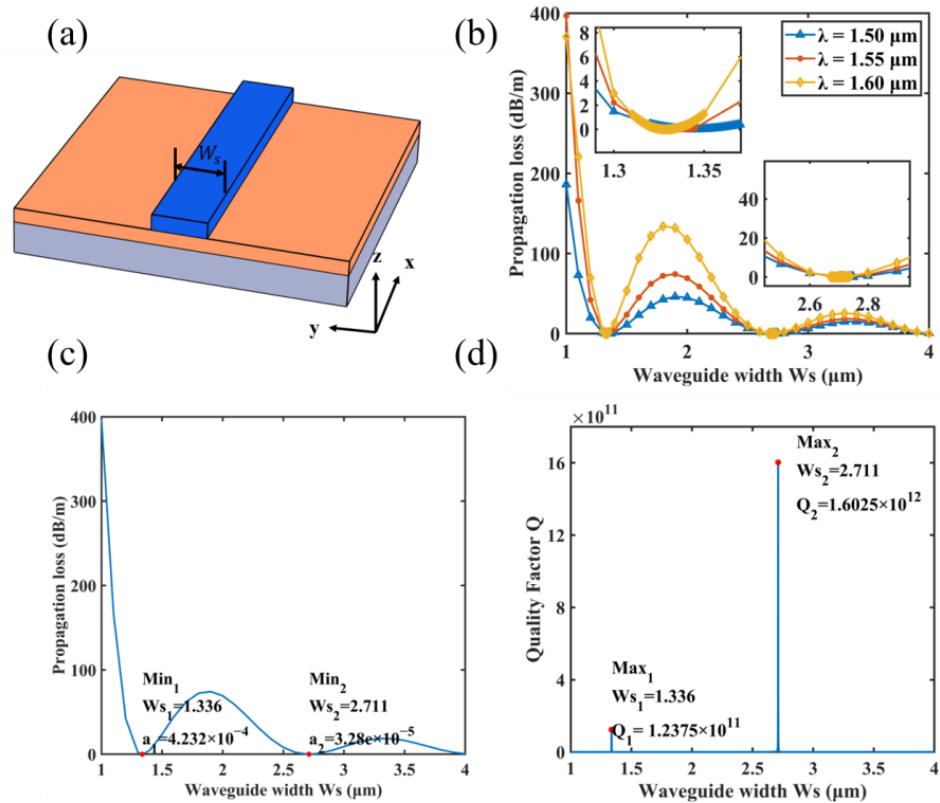
Figure 6. Simulation of the optical properties of the BIC structure under the straight waveguide: (**a**) illustration of the straight waveguide structure supporting a BIC mode, where *Ws* denotes the width of the straight waveguide; (**b**) the variation curve of propagation loss with waveguide width *Ws* at different wavelengths in the straight waveguide shown in (**a**) is simulatedl (**c**) the propagation loss curve of the straight waveguide at 1.55 μm wavelength as a function of waveguide width *Ws*; (**d**) the quality factor of the straight waveguide as a function of waveguide width *Ws* at the wavelength of 1.55 μm.

Figure 6a shows the hybrid straight waveguide BIC structure using a polymer waveguide on a high-refractive-index Si film, where *Ws* represents the width of the straight waveguide. The blue, red, and orange curves in Figure 6b represent the variation of propagation loss with the straight waveguide width *Ws* at the wavelength of 1.50 μm, 1.55 μm, and 1.60 μm, respectively. As shown in Figure 6b, the TM bound mode maintains ultra-low loss over a wide wavelength range. When the straight waveguide width is near 1.3 μm and 2.7 μm, the propagation loss is close to zero, which is the BIC structure we desired. In order to find the lowest loss point, we swept the reference at 1 nm spacing around the waveguide width of 1.3 μm and 2.7 μm. The two insets in the figure are zoomed in on the vicinity of the two BIC points in order to more clearly observe the trend of change near the two BIC points.

Figure 6c simulates the propagation loss curve of the TM bound mode in the straight waveguide as a function of waveguide width *Ws* when the light wavelength is 1.55 μm, showing the loss rate of the TM bound mode propagating in the straight waveguide, where the loss is a function of waveguide width *Ws* and wavelength λ. There are two BIC points in the range of 1–4 μm waveguide width, that is, the propagation loss of the BIC straight waveguide is 4.232×10^{-4} dB/m at 1.336 μm, and the propagation of the BIC straight waveguide is 3.28×10^{-5} dB/m at 2.711 μm. Figure 6d simulates the quality factor as a function of the straight waveguide width *Ws* for the wavelength of 1.55 μm. Two BIC points correspond to the largest Q values of 1.2375×10^{11} and 1.6025×10^{12}, respectively.

3.2. BIC in a Bent Waveguide

Bent waveguides are often used as connections between components of the same integrated chip and can also be used to change the direction of optical transmission. In the design of integrated optical devices, keeping the waveguide bending radius as small as possible is desirable to reduce the device's size. However, when the bending radius is too small, the radiation loss of the optical field energy will occur in the bent part of the waveguide, which can be ignored only when the bending radius of the bent waveguide is large enough. On the estimation of scattering losses due to sidewall roughness in bending optical waveguides, Ciminelli, C. et al. propose a three-dimensional mode solver based on the mode matching method to calculate the optical field distribution over the cross section of a bending waveguide. The method is based on the bulk current method (VCM) [42]. In order to find the appropriate bending radius, we used the angle-preserving transformation method proposed by K. Thyagarajan to simulate the BIC in a bent waveguide [43]. It involves equating a bent waveguide structure with a uniform refractive index distribution into a straight waveguide structure with the refractive index distribution varying in the direction of the bend. Then, the straight waveguide is analyzed to obtain the bending loss. To obtain the loss characteristics of the bent waveguide, we simulated and analyzed the optical properties of the BIC structure under a bent waveguide in the same way as the above straight waveguide.

Figure 7a shows the hybrid bent waveguide BIC structure using a polymer waveguide on a high-refractive-index Si film, where *Wb* represents the width of the waveguide, and *Rb* denotes the bending radius of the waveguide. Figure 7b simulates the propagation loss with bend radius *Rb* at different wavelengths in the bent waveguide when the waveguide width is 1.336 µm. The simulation results show that the propagation loss of the bent waveguide decays exponentially with increasing bending radius and changes more slowly as it increases to 500 µm. The variation of the loss profile with radius is essentially the same at three different wavelengths, implying that the TM bound mode also maintains ultra-low losses over a wide wavelength range in the bent waveguide. The simulation results are in high agreement with the theory. In addition to losses, we also consider the chip size, so we will take the radius *Rb* to be 500 µm as the following structural design parameters.

Different from the straight waveguide mentioned above, the propagation loss of the bent waveguide is also related to the bending radius, where the loss is a function of waveguide width *Wb*, wavelength λ, and bending radius *Rb*. Figure 7c,d simulate the propagation loss and quality factor curves of the TM bound mode in the bent waveguide as a function of waveguide width *Wb* when the wavelength λ and bending radius *Rb* are 1.55 µm and 500 µm, respectively. When the bent waveguide width is 1.336 µm, the loss at the first BIC point is 0.0055 dB/m, and the quality factor is 9.498×10^9; when the bent waveguide width is 2.714 µm, the loss at the second BIC point is 0.05457 dB/m, and the quality factor is 9.623×10^8. Due to the presence of waveguide bending, the propagation loss values obtained from the simulation are greater than those of a straight waveguide, and there is a drop in the quality factor (Q).

Through the simulation of the BIC straight waveguide and the BIC bent waveguide, we can find from the simulation results that there is a minimum transmission loss of both the straight waveguide and bent waveguide under the same waveguide width to obtain an ideal BIC. We take the waveguide width w of 1.336 µm as an essential structural parameter for designing a passive sensitive waveguide loop. After the simulation of the BIC in a bent waveguide, another parameter bending radius Rb was taken to be 500 µm, as continuing to increase the radius has no significant change in loss and is not conducive to miniaturization of the optical gyroscope system.
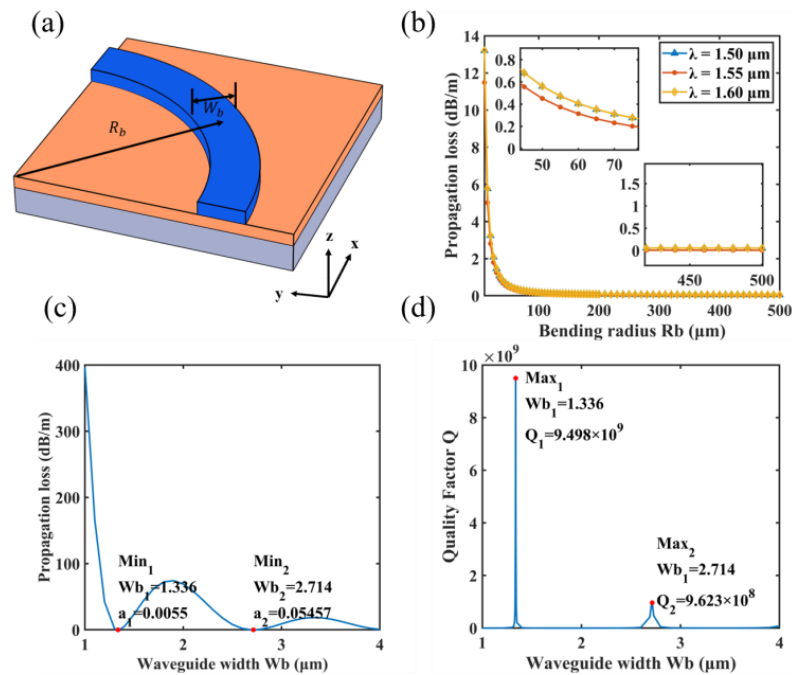
Figure 7. Simulation of the optical properties of the BIC structure under the bent waveguide: (**a**) illustration of the bent waveguide structure supporting a BIC mode, where *Wb* and *Rb* denote the width and radius of the bent waveguide, respectively; (**b**) the variation curve of propagation loss with bending radius *Rb* at different wavelengths in the bent waveguide shown in (**a**) is simulated when the waveguide width is 1.336 μm; (**c**) the propagation loss curve of the bent waveguide at 1.55 μm wavelength as a function of waveguide width *Wb* when the bending radius *Rb* is 500 μm; (**d**) the quality factor of the bent waveguide as a function of waveguide width *Wb* at the wavelength of 1.55 μm when the bending radius *Rb* is 500 μm.

Figure 8 show the variation curve of propagation loss with the thickness of SiO$_2$ at different wavelengths in the BIC straight waveguide when the waveguide width is 1.336 μm. By performing a parameterized scan of the SiO$_2$ thickness, it can be clearly observed that the propagation loss decreases with the increase of thickness *H*. This is due to the fact that increasing thickness allows for better constraint of the mode energy. By continuing to increase *H* up to 2 um, further increases in *H* have little effect on the results and have ultra-low loss values for a wide range of wavelengths.
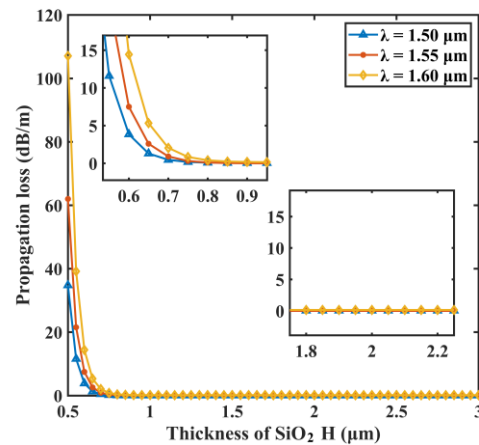

Figure 8. The variation curves of propagation loss with the thickness of SiO$_2$ *H* at different wavelengths in the BIC straight waveguide is simulated when the waveguide width is 1.336 μm.

Figure 9a,b show the cross-section mode field distributions for the BIC straight waveguide and the BIC bent waveguide, respectively. It can be seen from the figure that the mode field energy in the BIC straight waveguide is mainly limited to the high-refractive Si thin film below the polymer waveguide. The mode field of the BIC bent waveguide in Figure 7b causes the energy leakage of the optical field at the outside of the waveguide due to the left bending of the waveguide, which results in bending loss.
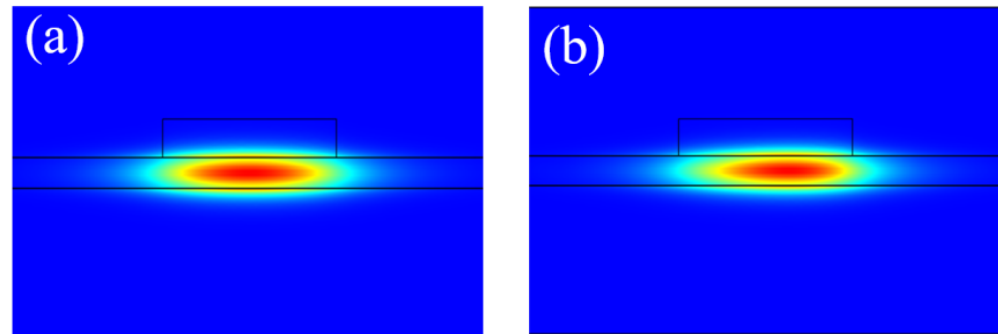

Figure 9. Cross-section mode field distribution of (**a**) a BIC straight waveguide and (**b**) a BIC bent waveguide.

3.3. Dispersion Effects at a Single Wavelength

Dispersion effect usually refers to the propagation of light waves in a medium, where different frequencies of light waves have different phase velocities due to the dispersion properties of the medium, resulting in a change in their phase. Dispersion has a significant impact on the performance of optical gyroscopes. Besides in a vacuum, every medium has its specific dispersion characteristics. A single wavelength can also exhibit dispersion effects under different structural parameters. In our simulations of BIC waveguides, the effect of dispersion is taken into account. Figure 10 reflects the dispersion effect at a single wavelength. The real and imaginary parts of the effective refractive index vary with the structural parameters. The real part increases with the width of the waveguide, and the imaginary part reflects the loss characteristics of the BIC waveguide. When the bending radius is set to 500 μm, the dispersion curves of straight and bent waveguides vary consistently as a whole. We have taken dispersion effects into account when calculating the Q-factor of the BIC waveguide structure.

3.4. Design of Archimedes Spiral Waveguide Coil

As the core sensitive component of the integrated optical gyroscope, the performance of the passive sensitive loop directly affects the sensitivity of the gyroscope. The design goal of the integrated waveguide sensing coil is to achieve the largest coil area and the lowest loss possible, which is used to improve the performance of the integrated optical gyroscope. Figure 11 shows the design diagram of the integrated waveguide sensing coil. The structure consists of two straight waveguides supporting the BIC mode and several bent waveguides supporting BIC modes connected at the same waveguide width to form an Archimedean spiral waveguide structure supporting the BIC mode. The two straight waveguides in the spiral structure serve as the input and output waveguides, and the straight waveguide on the left passes through a semicircle to achieve a smooth transition. When the radius is large enough (500 μm) to give negligible perturbation to the mode, the waveguide crossings can be equivalent to straight-straight crossings.
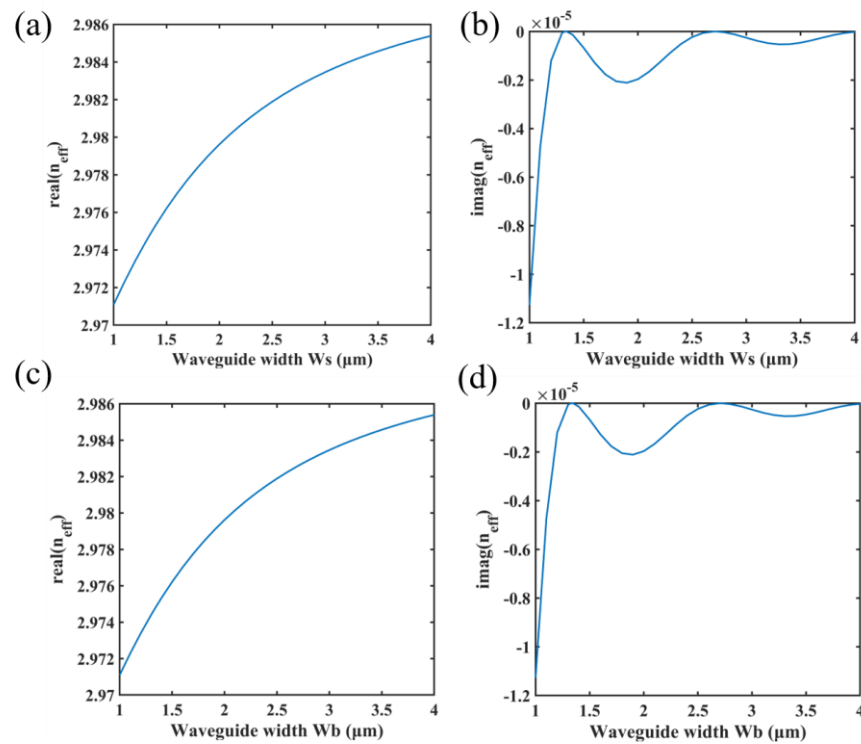
Figure 10. Dispersion effects at a single wavelength: variation of the real (**a**) and imaginary parts (**b**) of the effective refractive index with the width of the waveguide of a straight waveguide at a wavelength of 1.55um, the real (**c**) and imaginary parts (**d**) of the effective refractive index curve of the bent waveguide at 1.55 μm wavelength as a function of waveguide width *Wb* when the bending radius *Rb* is 500 μm.
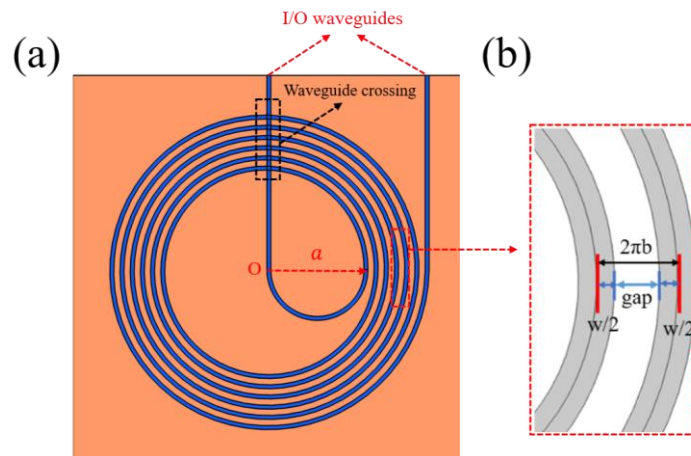

Figure 11. (**a**) Diagram of the Archimedes spiral structure designed as a passive sensitive gyroscope; (**b**) instructions for setting parameters between adjacent waveguide structures.

The Archimedes structure is a spiral structure with a fixed distance between adjacent waveguides, which can achieve the maximum enclosed area and length under a given chip footprint. The polar equation of the Archimedean spiral is defined as:

$$\rho = a + b\theta \tag{8}$$

where *a* is the initial radius of the spiral, *b* represents the increase of the pole diameter at each rotation degree, and the distance between adjacent spiral coils is $2\pi b$. When the waveguide width is *w*, the distance between adjacent spiral coils can be expressed as the

sum of the width of the spiral waveguide and the *gap* between adjacent waveguides, i.e., $2\pi b = w + gap$.

The total length enclosed by the Archimedes spiral waveguide is given by:

$$L_n = \int_0^{2N\pi} \sqrt{\rho^2 + \rho'^2} \, d\theta = \int_0^{2N\pi} \sqrt{(a^2 + 2ab\theta + b^2\theta^2 + b^2)} \, d\theta \qquad (9)$$

The effective area enclosed by the Archimedean spiral waveguide is given by:

$$A_n = \int_0^{2N\pi} \frac{1}{2}\rho^2 \, d\theta = N\pi \left[a^2 + 2N\pi ab + \frac{(2N\pi b)^2}{3} \right] \qquad (10)$$

In order to meet the need for the miniaturization of the integrated optical gyroscope and to consider the effect of bending radius on waveguide losses, we set the initial radius of the spiral *a* to 500 μm in our model structure. We set the waveguide width *w* of another parameter in the structure to 1.336 μm. At this time, the straight waveguide and the bent waveguide of the structure satisfy the BIC condition simultaneously and have the lowest loss value. Based on the design of ultra-low-loss waveguide crossing arrays in the literature [39] and combined with the mode field distribution of our simulation, the gap between adjacent waveguides is set as 4 μm, which is determined based on our design and theoretical simulations, taking into account manufacturing process limitations. This value not only allows for miniaturisation, but also guarantees the performance and manufacturing feasibility of the device.

4. Discussion

We have summarized the performance parameters of some other integrated optical material platforms reported in the literature, as shown in Table 1. The comparison shows that our waveguide structures designed using BIC have lower losses and higher Q values than any of the materials that have been reported so far. The loss value is two orders of magnitude lower than the currently reported low-loss GaF_2 waveguide. We use the optical characteristics of high Q value and low loss in the BIC structure to design the sensitive parts of the optical gyroscope and improve its performance of the gyroscope.

Table 1. Comparison of property of integrated optical material platforms reported in the other literature.

Reference	Material	Propagation Loss	Q Factor
[10]	InP	0.45 dB/cm	10^6
[13]	SOI	1.328 dB/cm	\
[17]	Si_3N_4	7.8×10^{-3} dB/cm	10^8
[21]	SiO_2	5.0×10^{-3} dB/cm	10^9
[25]	Polymer	0.5 dB/cm	10^5
[27]	$LiNbO_3$	2.7×10^{-2} dB/cm	10^7
[29]	GaF_2	1×10^{-4} dB/cm	10^{10}
This Work	BIC	4.232×10^{-6} dB/cm	10^{11}

The limiting sensitivity is a vital indicator parameter for the performance of the integrated optical gyroscope, which is generally expressed as the minimum detectable angular velocity of the gyroscope under the condition of shot noise limitation [44]. Setting the phase bias of the gyroscope to $\pi/2$, which is the best bias point of the gyroscope sensitivity, the sensitivity formula of the gyroscope can be estimated by the following expression:

$$\delta\Omega = \frac{c}{8A_n} \sqrt{\frac{Bhc\lambda}{\eta P_{Di}}} \times \frac{180}{\pi} \ (\text{deg}/s) \qquad (11)$$

In the above formula, c denotes the speed of light in a vacuum, A_n represents the effective area enclosed by the designed Archimedean spiral waveguide, B is the detection bandwidth, h is the Planck constant, η is the efficiency of the photodetector, and λ is the operating wavelength. The initial setting parameters for simulation in this paper are shown in Table 2.

Table 2. Initial setting parameters setting.

Symbol	Parameter	Value
λ	Operating wavelength	1.55 μm
c	Speed of light in vacuum	3×10^8 m/s
B	Detection bandwidth	20 Hz
h	Planck constant	6.626×10^{-34} J·s
η	Photodetector efficiency	0.9
P_0	Input optical power	10 mW

The structural parameters for the integrated sensitive waveguide coil design were determined by simulating the optical properties of the BIC waveguide. Our paper uses shot-noise-limited sensitivity as the standard for evaluating the performance of the gyroscope. Taking the obtained parameters and the initial parameter settings given in Table 2 into Equation (11), we can obtain a performance diagram for the gyroscope. Figure 12 shows the variation of the gyroscope shot-noise-limit sensitivity with the number of turns of the spiral waveguide coil. In order to more clearly find the number of turns corresponding to the optimum performance, we enlarged the position of $N = 239$. The curve shows that the value of the gyroscope sensitivity decreases as the number of turns of the coil increases; the smaller the value, the better the performance. When N is small, the effect of loss on performance is smaller than that of increasing area. Thus, with the increase of N, the sensitivity decreases, and the performance becomes better. When $N = 239$, there is a turning point where the sensitivity value reaches its minimum, and the performance is optimal. With a further increase of N, the effect of loss on performance exceeds that of increasing the area, causing the sensitivity value to increase and the performance to gradually decrease. Therefore, the number of turns $N = 239$ corresponding to the minimum sensitivity of the gyroscope is the optimal number for performance, and the sensitivity at this point is 0.6699 deg/s. Further increasing the number of turns N, the performance of the gyroscope decreases and is not conducive to the miniaturization of the device. The interferometric integrated optical gyroscope performance we designed based on the BIC waveguide is 12 times that in Ref. [13].
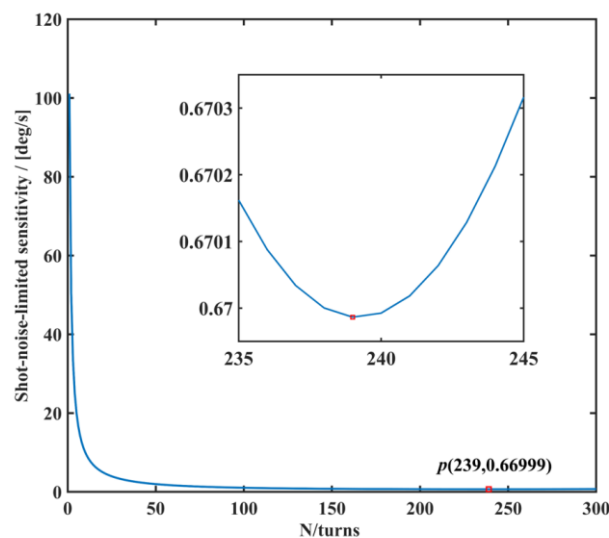

Figure 12. Variation of gyroscope sensitivity with the number of turns of the waveguide coil.

5. Conclusions

In summary, to solve the problem that the performance of gyroscopes is severely limited by the high loss of conventional optical waveguides and the difficulty of designing long optical waveguide coils, we designed a novel idea of an ultra-low-loss Archimedean spiral waveguide structure used for an on-chip integrated optical gyroscope by combining the unique properties of optical BIC. The sensitivity of the integrated optical gyroscope is related to the total area enclosed by each encircling spiral waveguide. By designing the Archimedes spiral waveguide structure, the relatively small winding length of the low-loss spiral coil forms a large effective area, making it possible for the micro-sensor to measure low rotational speeds. We also investigated its optical properties by using the FEM. The simulation result shows that the propagation loss, Q factor, and gyroscope sensitivity are 4.232×10^{-6} dB/cm, 10^{11}, and $0.6699°/s$, respectively. Compared with the traditional integrated optical material platform, the propagation loss of the designed BIC waveguide structure is significantly reduced, and the quality factor is also greatly improved, thereby improving the sensitivity of the gyroscope. Since this optical waveguide structure does not need to etch optical functional materials with high refractive indices, this work also effectively solves the etching problem of single crystal materials on various integrated optical chips. This is the first time a BIC optical waveguide has been used in an integrated optical gyroscope and for providing a good solution for developing miniaturized integrated optical gyroscopes.

Institutional Review Board Statement: Not applicable.

Informed Consent Statement: Not applicable.

Data Availability Statement: Data are available in the main text.

Conflicts of Interest: The authors declare no conflict of interest.

References

1. Ezekiel, S.; Balsamo, S. Passive ring resonator laser gyroscope. *Appl. Phys. Lett.* **1977**, *30*, 478–480. [CrossRef]
2. Venediktov, V.Y.; Filatov, Y.V.; Shalymov, E.V. Passive ring resonator micro-optical gyroscopes. *Quantum Electron.* **2016**, *46*, 437. [CrossRef]
3. Chow, W.; Gea-Banacloche, J.; Pedrotti, L.; Sanders, V.; Schleich, W.; Scully, M. The ring laser gyro. *Rev. Mod. Phys.* **1985**, *57*, 61. [CrossRef]
4. Culshaw, B.; Giles, I. Fibre optic gyroscopes. *J. Phys. E Sci. Instrum.* **1983**, *16*, 5. [CrossRef]
5. Khial, P.P.; White, A.D.; Hajimiri, A. Nanophotonic optical gyroscope with reciprocal sensitivity enhancement. *Nat. Photonics* **2018**, *12*, 671–675. [CrossRef]
6. Xue, X.-M.; Tang, J.; Zhou, H.-L.; Qin, Y.-Y.; Song, Y.; Li, R.-Z.; Zhang, X.-Y.; Zhang, T. All-polymer monolithic resonant integrated optical gyroscope. *Opt. Express* **2022**, *30*, 42728–42737. [CrossRef]
7. Suzuki, K.; Takiguchi, K.; Hotate, K. Monolithically integrated resonator microoptic gyro on silica planar lightwave circuit. *J. Light. Technol.* **2000**, *18*, 66–72. [CrossRef]
8. Gundavarapu, S.; Huffman, T.; Moreira, R.; Belt, M.; Bowers, J.E.; Blumenthal, D.J. Integrated ultra-low-loss silicon nitride waveguide coil for optical gyroscopes. In Proceedings of the Optical Fiber Communication Conference, Anaheim, CA, USA, 20–24 March 2016; p. W4E. 5.

9.   Horikawa, T.; Shimura, D.; Mogami, T. Low-loss silicon wire waveguides for optical integrated circuits. *MRS Commun.* **2016**, *6*, 9–15. [CrossRef]

10.   Ciminelli, C.; Dell'Olio, F.; Armenise, M.N.; Soares, F.M.; Passenberg, W. High performance InP ring resonator for new generation monolithically integrated optical gyroscopes. *Opt. Express* **2013**, *21*, 556–564. [CrossRef]

11.   Ciminelli, C.; D'Agostino, D.; Carnicella, G.; Dell'Olio, F.; Conteduca, D.; Ambrosius, H.P.; Smit, M.K.; Armenise, M.N. A high-Q InP resonant angular velocity sensor for a monolithically integrated optical gyroscope. *IEEE Photonics J.* **2015**, *8*, 6800418. [CrossRef]

12.   He, Y.; Lu, Z.; Kuai, X.; Feng, Z.; Han, W.; Li, Z.; Yan, W.; Yang, F. Heterogeneous integration of InP and Si3N4 waveguides based on interlayer coupling for an integrated optical gyroscope. *Appl. Opt.* **2021**, *60*, 662–669. [CrossRef]

13.   Wu, B.; Yu, Y.; Xiong, J.; Zhang, X. Silicon integrated interferometric optical gyroscope. *Sci. Rep.* **2018**, *8*, 8766. [CrossRef]

14.   Wu, B.; Yu, Y.; Zhang, X. Mode-assisted Silicon integrated interferometric optical Gyroscope. *Sci. Rep.* **2019**, *9*, 12946. [CrossRef] [PubMed]

15.   Lim, A.E.-J.; Song, J.; Fang, Q.; Li, C.; Tu, X.; Duan, N.; Chen, K.K.; Tern, R.P.-C.; Liow, T.-Y. Review of silicon photonics foundry efforts. *IEEE J. Sel. Top. Quantum Electron.* **2013**, *20*, 405–416. [CrossRef]

16.   Tien, M.-C.; Bauters, J.F.; Heck, M.J.; Spencer, D.T.; Blumenthal, D.J.; Bowers, J.E. Ultra-high quality factor planar Si3N4 ring resonators on Si substrates. *Opt. Express* **2011**, *19*, 13551–13556. [CrossRef]

17.   Gundavarapu, S.; Belt, M.; Huffman, T.A.; Tran, M.A.; Komljenovic, T.; Bowers, J.E.; Blumenthal, D.J. Interferometric optical gyroscope based on an integrated Si3N4 low-loss waveguide coil. *J. Light. Technol.* **2017**, *36*, 1185–1191. [CrossRef]

18.   El Dirani, H.; Youssef, L.; Petit-Etienne, C.; Kerdiles, S.; Grosse, P.; Monat, C.; Pargon, E.; Sciancalepore, C. Ultralow-loss tightly confining Si3N4 waveguides and high-Q microresonators. *Opt. Express* **2019**, *27*, 30726–30740. [CrossRef]

19.   Huffman, T.; Davenport, M.; Belt, M.; Bowers, J.E.; Blumenthal, D.J. Ultra-low loss large area waveguide coils for integrated optical gyroscopes. *IEEE Photonics Technol. Lett.* **2016**, *29*, 185–188. [CrossRef]

20.   Bauters, J.F.; Heck, M.J.; John, D.; Dai, D.; Tien, M.-C.; Barton, J.S.; Leinse, A.; Heideman, R.G.; Blumenthal, D.J.; Bowers, J.E. Ultra-low-loss high-aspect-ratio Si3N4 waveguides. *Opt. Express* **2011**, *19*, 3163–3174. [CrossRef] [PubMed]

21.   Liu, D.; Li, H.; Wang, X.; Liu, H.; Ni, P.; Liu, N.; Feng, L. Interferometric optical gyroscope based on an integrated silica waveguide coil with low loss. *Opt. Express* **2020**, *28*, 15718–15730. [CrossRef] [PubMed]

22.   Zhang, J.; Ma, H.; Li, H.; Jin, Z. Single-polarization fiber-pigtailed high-finesse silica waveguide ring resonator for a resonant micro-optic gyroscope. *Opt. Lett.* **2017**, *42*, 3658–3661. [CrossRef] [PubMed]

23.   Li, J.; Suh, M.-G.; Vahala, K. Microresonator brillouin gyroscope. *Optica* **2017**, *4*, 346–348. [CrossRef]

24.   Feng, L.; Wang, J.; Zhi, Y.; Tang, Y.; Wang, Q.; Li, H.; Wang, W. Transmissive resonator optic gyro based on silica waveguide ring resonator. *Opt. Express* **2014**, *22*, 27565–27575. [CrossRef] [PubMed]

25.   Qian, G.; Zhang, T.; Zhang, L.-J.; Tang, J.; Zhang, X.-Y.; Lu, Y.; Wan, F.-H. Demonstrations of centimeter-scale polymer resonator for resonant integrated optical gyroscope. *Sens. Actuators A Phys.* **2016**, *237*, 29–34. [CrossRef]

26.   Liu, J.; Yu, L.; Wu, J. Optical Gyroscope Based on Multi-gap Surface Plasmon Optical Waveguide. *J. Appl. Sci. Eng.* **2019**, *22*, 299–306.

27.   Zhang, M.; Wang, C.; Cheng, R.; Shams-Ansari, A.; Lončar, M. Monolithic ultra-high-Q lithium niobate microring resonator. *Optica* **2017**, *4*, 1536–1537. [CrossRef]

28.   Vannahme, C.; Suche, H.; Reza, S.; Ricken, R.; Quiring, V.; Sohler, W. Integrated optical Ti: LiNbO3 ring resonator for rotation rate sensing. In Proceedings of the 13th ECIO 2007, Copenhagen, Denmark, 25–27 April 2007.

29.   Savchenkov, A.A.; Matsko, A.B.; Ilchenko, V.S.; Maleki, L. Optical resonators with ten million finesse. *Opt. Express* **2007**, *15*, 6768–6773. [CrossRef]

30.   Savchenkov, A.A.; Liang, W.; Ilchenko, V.; Matsko, A.; Maleki, L. Crystalline waveguides for optical gyroscopes. *IEEE J. Sel. Top. Quantum Electron.* **2018**, *24*, 1–11. [CrossRef]

31.   Brunetti, G.; Dell'Olio, F.; Conteduca, D.; Armenise, M.N.; Ciminelli, C. Comprehensive mathematical modelling of ultra-high Q grating-assisted ring resonators. *J. Opt.* **2020**, *22*, 035802. [CrossRef]

32.   Liu, K.; Jin, N.; Cheng, H.; Chauhan, N.; Puckett, M.W.; Nelson, K.D.; Behunin, R.O.; Rakich, P.T.; Blumenthal, D.J. Ultralow 0.034 dB/m loss wafer-scale integrated photonics realizing 720 million Q and 380 μW threshold Brillouin lasing. *Opt. Lett.* **2022**, *47*, 1855–1858. [CrossRef]

33.   Yu, Z.; Xi, X.; Ma, J.; Tsang, H.K.; Zou, C.-L.; Sun, X. Photonic integrated circuits with bound states in the continuum. *Optica* **2019**, *6*, 1342–1348. [CrossRef]

34.   Yu, Z.; Sun, X. Acousto-optic modulation of photonic bound state in the continuum. *Light Sci. Appl.* **2020**, *9*, 1. [CrossRef] [PubMed]

35.   Zou, C.L.; Cui, J.M.; Sun, F.W.; Xiong, X.; Zou, X.B.; Han, Z.F.; Guo, G.C. Guiding light through optical bound states in the continuum for ultrahigh-Q microresonators. *Laser Photonics Rev.* **2015**, *9*, 114–119. [CrossRef]

36.   Qin, H.; Shi, X.; Ou, H. Exceptional points at bound states in the continuum in photonic integrated circuits. *Nanophotonics* **2022**, *11*, 4909–4917. [CrossRef]

37.   Post, E.J. Sagnac effect. *Rev. Mod. Phys.* **1967**, *39*, 475. [CrossRef]

38.   Feng, Z.; He, Y.; Yan, W.; Yang, F.; Han, W.; Li, Z. Progress of waveguide ring resonators used in micro-optical gyroscopes. In Proceedings of the Photonics, 2020, Online, 29 September–1 October 2020; p. 96.

39. Liu, Y.; Shainline, J.M.; Zeng, X.; Popović, M.A. Ultra-low-loss CMOS-compatible waveguide crossing arrays based on multimode Bloch waves and imaginary coupling. *Opt. Lett.* **2014**, *39*, 335–338. [CrossRef]
40. White, T.; Kuhlmey, B.; McPhedran, R.; Maystre, D.; Renversez, G.; De Sterke, C.M.; Botten, L. Multipole method for microstructured optical fibers. I. Formulation. *JOSA B* **2002**, *19*, 2322–2330. [CrossRef]
41. Hsu, C.W.; Zhen, B.; Stone, A.D.; Joannopoulos, J.D.; Soljačić, M. Bound states in the continuum. *Nat. Rev. Mater.* **2016**, *1*, 16048. [CrossRef]
42. Ciminelli, C.; Passaro, V.M.; Dell'Olio, F.; Armenise, M.N. Three-dimensional modelling of scattering loss in InGaAsP/InP and silica-on-silicon bent waveguides. *J. Eur. Opt. Soc.-Rapid Publ.* **2009**, *4*, 09015. [CrossRef]
43. Thyagarajan, K.; Shenoy, M.; Ghatak, A.K. Accurate numerical method for the calculation of bending loss in optical waveguides using a matrix approach. *Opt. Lett.* **1987**, *12*, 296–298. [CrossRef]
44. Ciminelli, C.; Dell'Olio, F.; Campanella, C.E.; Armenise, M.N. Photonic technologies for angular velocity sensing. *Adv. Opt. Photonics* **2010**, *2*, 370–404. [CrossRef]